A&A 673, L8 (2023)
https://doi.org/10.1051/0004-6361/202346384

Astronomy & Astrophysics

LETTER TO THE EDITOR

Solar energetic particle event onsets at different heliolongitudes: The effect of turbulence in Parker spiral geometry

T. Laitinen, S. Dalla, C. O. G. Waterfall, and A. Hutchinson

Jeremiah Horrocks Institute, University of Central Lancashire, Corporation Street, PR1 2HE Preston, UK
e-mail: tlmlaitinen@uclan.ac.uk

Received 11 March 2023 / Accepted 20 April 2023

ABSTRACT

Context. Solar energetic particles (SEPs), accelerated during solar eruptions, are observed to rapidly reach a wide heliolongitudinal range in the interplanetary space. Turbulence-associated SEP propagation across the mean Parker spiral direction has been suggested to contribute to this phenomenon.
Aims. We study SEP propagation in turbulent magnetic fields to evaluate SEP spatial distribution in the heliosphere, their path lengths, and the overall evolution of SEP intensities at 1 au.
Methods. We use full-orbit test particle simulations of 100-MeV protons in a novel analytic model of the turbulent heliospheric magnetic field, where the turbulence is dominated by modes that are transverse and 2D with respect to the Parker spiral direction.
Results. We find that by propagating along meandering field lines, SEPs reach a 60°-wide heliolongitudinal range at 1 au within an hour of their injection for the turbulence parameters considered. The SEP onset times are asymmetric with respect to the location connected to the source along the Parker spiral, with the earliest arrival times being 15° westwards from the well-connected Parker spiral longitude. The inferred path length of the first arriving particles is 1.5−1.8 au within 30° of the well-connected longitude; 20−30% longer than the length of the random-walking field lines, increasing monotonously at longitudes further away; and 30−50% longer than the Parker spiral. The global maximum intensity is reached 15° west from the well-connected longitude an hour after the SEP injection. Subsequently, the SEP distribution broadens, consistent with diffusive spreading of SEPs across the field lines.
Conclusions. Our results indicate that magnetic field line meandering can explain rapid access of SEPs to wide longitudinal ranges, as well as several other features of SEP event intensity evolution.

Key words. Sun: particle emission – Sun: heliosphere – magnetic fields – turbulence – methods: numerical

1. Introduction

Solar energetic particles (SEPs) are accelerated during solar eruptions. The acceleration processes of SEPs are typically divided into flare-related processes and those related to the shock wave driven by coronal mass ejections (CMEs) in the corona and interplanetary space. The SEP events are traditionally classified as impulsive or gradual, with the impulsive, flare-related events being small, short-lived, rich in heavy elements, and narrow in heliolongitudinal extent, whereas the gradual, proton-rich events are seen at a wide range of heliolongitudes, and can last for up to over a week (e.g. Reames 1999). This classification has been challenged particularly by the recent multi-spacecraft observations of heavy element-rich SEP events that have a wide heliolongitudinal extent (Wiedenbeck et al. 2013; Cohen et al. 2014, 2017), similar to typical gradual SEP event extents (e.g. Lario et al. 2006, 2013; Richardson et al. 2014). Several ideas have been presented to explain the observation of heavy elements over broad regions in heliolongitude, such as coronal spreading of magnetic field lines (e.g. Liewer et al. 2004), sympathetic flaring (e.g. Schrijver & Title 2011), reacceleration of remnant flare particles by CME-driven shock waves (e.g. Mason et al. 1999; Reames 1999; Desai et al. 2003), and cross-field propagation of SEPs in the interplanetary space due to solar wind turbulence.

The effect of turbulence on SEP propagation in the interplanetary space is typically described as pitch angle diffusion along and spatial diffusion across the mean Parker spiral direction (e.g. Parker 1958; Jokipii 1966). Earlier modelling of SEP observations concentrated on SEP propagation along the mean Parker spiral (e.g. Kallenrode 1993; Torsti et al. 1996; Dröge 2000; Agueda et al. 2009) as, based on the so-called Palmer consensus (Palmer 1982), the cross-field effects due to turbulence were considered negligible.

Recently, the significance of stochastic cross-field propagation of SEPs has gained more attention. Most models have concentrated on studying the effects of the turbulence by describing them as diffusion across the mean field direction on SEP intensities (e.g. Zhang et al. 2009; Dröge et al. 2010; He et al. 2011; Strauss & Fichtner 2015). However, Laitinen et al. (2013) note that in the timescales of propagation to Earth, the early transport of SEPs is dominated by deterministic propagation along stochastically meandering field lines, rather than stochastic motion relative to the mean magnetic field. Laitinen et al. (2016) implemented this new description of transport into a Fokker-Planck equation framework combining field line and particle diffusion, and they show that the combination of the initial deterministic propagation and time-asymptotic cross field diffusion resulted in a particle population that extended rapidly to a wide range of longitudes. Subsequently, the modelled SEP event

continued to broaden in heliolongitude at a slower pace, depending on turbulence strength (Laitinen et al. 2018).

The diffusion approach for particle or field line cross-field propagation is not able to address an important element of SEP transport: the length of the stochastically meandering field lines, which is crucial for connecting the solar SEP source to the analysis of the observed SEP onsets at the observing spacecraft. Long apparent path lengths of SEPs obtained from velocity dispersion analysis (VDA) have been reported in several studies (e.g. Paassilta et al. 2017, 2018; Leske et al. 2020). Recent simulation studies have shown that in general turbulence increases the mean length of interplanetary field lines (e.g. Pei et al. 2006; Moradi & Li 2019; Chhiber et al. 2021a). In Laitinen & Dalla (2019), we use a random-walk model to demonstrate that the lengthening of the field lines is asymmetric in heliolongitude, with longer field line lengths connecting an observer located east of the Parker spiral magnetic field connected to the field line source, as compared to a path connecting a westward observer. However, in that work, the field lines were modelled as stochastic random-walk instead of field lines that obey Maxwell's equations, and thus the nature of heliospheric turbulence was not fully taken into account.

More recently, we introduced a novel Parker spiral geometry turbulence model, where for the first time both the wave vectors and the fluctuating magnetic field vector of the dominant 2D turbulence component were normal to the Parker spiral background field (Laitinen et al. 2023). Analysis of field line lengths using this model agreed with the asymmetric distribution of field line lengths found by the random-walk model of Laitinen & Dalla (2019).

Our earlier work, described above, only investigated field line lengths, and did not include the effect of the turbulent magnetic field fluctuations on SEP propagation along the meandering field lines. For this Letter, we used full-orbit test particle simulations to trace SEP propagation in the Parker spiral turbulence model to investigate how turbulent fluctuations affect the arrival of the first particles to different longitudes at 1 au. From the simulations we derived the longitudinal dependence of onset and peak times of SEP intensities for comparison with observations (e.g. Lario et al. 2013; Richardson et al. 2014). We describe our model parameters and assumptions in Sect. 2, present our results in Sect. 3, and discuss their implications and draw our conclusions in Sect. 4.

2. Model

For this work, we integrated the full equation of motion of energetic particles from the source region near the Sun, and recorded the particles as they passed through a 1-au heliocentric sphere. We modified our Parker spiral full-orbit 3D test particle code (Dalla & Browning 2005; Marsh et al. 2013) to include, in addition to the Parker spiral field, a turbulent magnetic field component. The turbulence model, fully described in Laitinen et al. (2023), is dominated by a transverse 2D component where the wavenumber vector and the magnetic field vector are normal to each other, and normal to the background Parker spiral field. In addition to the 2D component, a slab-like component is also included. It should be emphasised that within the new version of the code, we do not include ad hoc pitch angle scattering as in the previous versions (e.g. Marsh et al. 2013): any changes in the particle velocity vector and position are solely due to the modelled magnetic field.

For this Letter, we used the same parametrisation of the solar wind and turbulence as in Laitinen et al. (2023). The Parker spiral magnetic field was parametrised by the magnetic field at $1\,r_\odot$ of 1.78 Gauss, the solar wind velocity $v_{\rm sw} = 400\,{\rm km\,s^{-1}}$, and solar angular rotation rate $\Omega = 2.86533 \times 10^{-6}\,{\rm rad\,s^{-1}}$. The 2D and slab components have been partitioned to have 80%:20% energy division. The spectra of both components have a flat energy-containing range between the largest scale $k_0 = 1/r$ and the breakpoint scales $\lambda_{\rm 2D}$ and $\lambda_{\rm slab}$, where r is the heliocentric distance, and the Kolmogorov spectrum above the breakpoint scales. As in Laitinen et al. (2023), we used $\lambda_\perp = 0.04(r/r_\odot)^{0.8}\,r_\odot$, $\lambda_{\rm slab} = 2\lambda_{\rm 2D}$, and $\delta B^2 = 0.03 B^2_{\rm p\odot}(r/r_\odot)^{-3.3}$, where $B_{\rm p\odot}$ is the magnitude of the Parker spiral magnetic field at $1\,r_\odot$. Recent observations suggest that the radial dependence of the 2D/slab ratio, the correlation scales, and the inertial spectral slopes may be more complicated than those used in this study (e.g. Chen et al. 2020; Bandyopadhyay & McComas 2021; Cuesta et al. 2022), as well as being different in different solar wind streams. These caveats are discussed further in Laitinen et al. (2023).

It should be noted that in this Letter, we include neither the convective solar wind electric field $\boldsymbol{E} = -\boldsymbol{v}_{\rm sw} \times \boldsymbol{B}$, where $\boldsymbol{v}_{\rm sw}$ is the solar wind velocity vector and $\boldsymbol{B}$ the background magnetic field, nor an electric field related to the turbulent fluctuations. For this reason, the particles retain their original energies, and do not experience the $\boldsymbol{E} \times \boldsymbol{B}$ drift which gives rise to the corotation drift (e.g. Dalla et al. 2013). The effects of convective and turbulent electric fields will be investigated in future work.

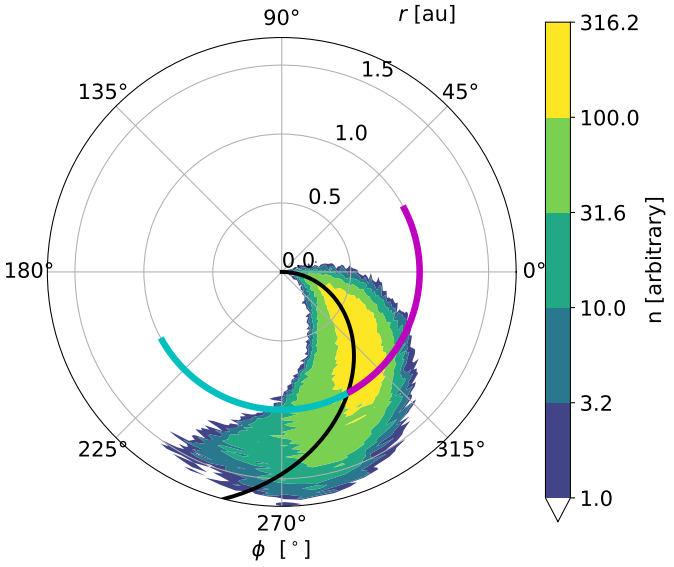

Fig. 1. Distribution of 100 MeV protons 1 h after injection from a 8°×8° source at the solar equator at $\phi = 0°$, integrated over latitude and binned in longitude and radius bins. The black curve shows the nominal Parker spiral originating from the centre of the source region. The magenta and cyan arcs at $r = 1$ au depict ranges for $\Delta\phi < 0°$ and $\Delta\phi > 0°$, respectively (see Eq. (1)).

3. Results

We simulated an impulsive injection of 100 000 100-MeV protons from a source of $8° \times 8°$ heliolongitudinal and heliolatitudinal area centred at the solar equator and heliolongitude $\phi_{\rm src} = 0°$ at $2\,r_\odot$ heliocentric distance. The protons were traced for 48 h as they propagated in the turbulent heliospheric magnetic field. In Fig. 1, we show the distribution of the particles, n, as counts integrated over latitude and binned over heliocentric distance and

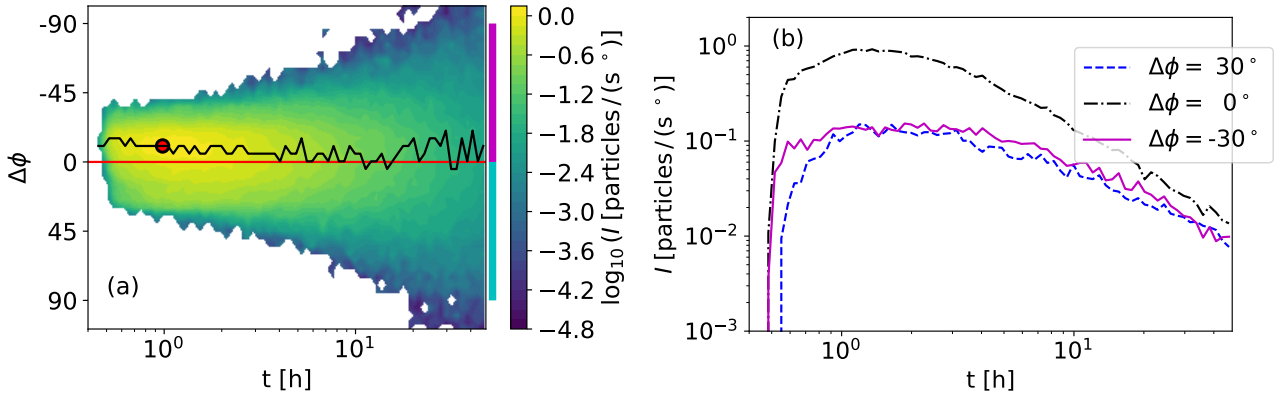

Fig. 2. Temporal evolution of 100-MeV proton intensities. (a) Contour of the intensity as a function of time and $\Delta\phi$ at 1 au. The horizontal red curve depicts the longitude of the footpoint centred at the particle source at $\phi_{\rm src}$, the black curve is the longitude where the intensity is at maximum at a given time, and the red circle shows the time and heliolongitude of the maximum intensity. The magenta and cyan ranges on the right correspond to those in Fig. 1. (b) Time evolution of the intensities at three heliolongitudes.

heliolongitude, after one hour of propagation. As we can see, the protons have spread from their original narrow 8° source to over a 60° heliolongitudinal range at 1 au, as a result of meandering magnetic field lines.

In Fig. 2, we investigate the temporal evolution of the heliolongitudinal particle intensity at 1 au. In Fig. 2a, we show a contour plot of the intensity $I(\phi, t)$ of the particles traversing through a 1-au sphere in units of particles/(s °) (integrated over latitude), as a function of time and relative heliolongitude

$$\Delta\phi = \phi_{\rm src} - \phi_{\rm fpt}, \tag{1}$$

where $\phi_{\rm fpt}$ is the footpoint longitude that connects an observer at (r, ϕ) to the solar surface along the Parker spiral magnetic field (the y-axis showing $\Delta\phi$ is inverted in Fig. 2a, to ease comparison with Fig. 1). For $v_{\rm sw} = 400\,{\rm km\,s^{-1}}$, the longitude at $r = 1$ au for which $\Delta\phi = 0°$ is $\phi_{1\,\rm au} = -61° = 299°$: that is, an observer at that longitude is connected to the source $\phi_{\rm src} = 0°$, along the black curve in Fig. 1. Observers located westwards from $\Delta\phi = 0°$ (magenta arc in Fig. 1 and vertical magenta bar in Fig. 2) have negative $\Delta\phi$, and vice versa for eastward observers (cyan arc and vertical bar). It should be noted that this definition of $\Delta\phi$ is consistent with that of Lario et al. (2013), whereas Richardson et al. (2014) use the opposite sign.

Figure 2a shows several interesting features of the particle distribution and its evolution in time. The particles arrive rapidly, within the first 35 min, to a ~60°-wide range in heliolongitude. The first particles arrive at around $\Delta\phi \approx -15°$, and the longitude at which the intensity is highest at any given time (black curve in Fig. 2a) tends to be westwards. The global maximum intensity is reached about 1 h after the injection of the particles, at $\Delta\phi = -10°$ (red circle in Fig. 2a). At later times, the particle population begins to broaden in heliolongitude, and after 48 h, the particles cover over 200° range of heliolongitudes, with the highest intensity at longitudes $\Delta\phi \approx 0°$ to $-5°$. It should be noted that as our model does not include the convective electric field, corotation effects on the SEP time-intensity profiles reported in Hutchinson et al. (2023) are not reproduced in our results. We also note that the mean colatitude of the particles evolves from the initial 75° to 85° during the 48 h simulation period (not shown), that is, the particles experience southward gradient and curvature drifts (Marsh et al. 2013; Dalla et al. 2013).

In Fig. 2b, we show the time-intensity profiles at three observers, one connected to the source at $\Delta\phi = 0°$ (dash-dotted black curve), one westwards at $\Delta\phi = -30°$ (solid magenta curve), and one eastwards at $\Delta\phi = 30°$ (dashed blue curve). The onset phase is clearly asymmetric: the intensity starts to rise simultaneously at $\Delta\phi = 0°$ and $\Delta\phi = -30°$, 4 min earlier than at $\Delta\phi = 30°$. Subsequently, the time-intensity profiles at the eastward and westward locations reach similar values, whereas the peak intensity at $\Delta\phi = 0°$ exceeds that of the eastward and westward locations by an order of magnitude.

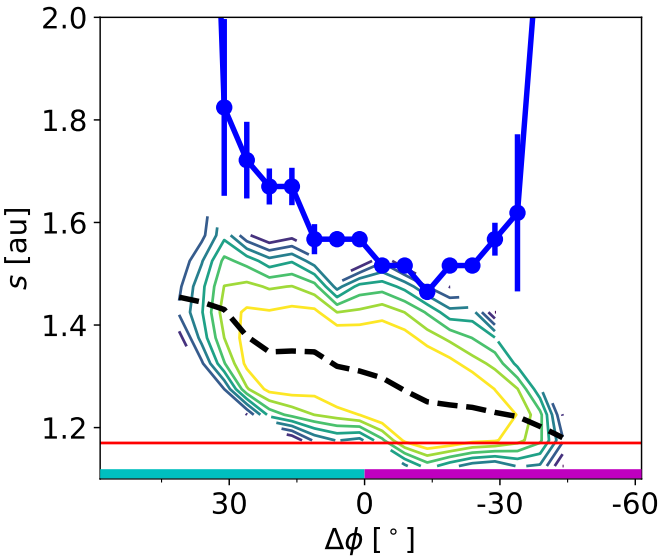

Fig. 3. Path lengths of the first arriving 100-MeV protons (thick blue curve) and the density of field lines (contour lines, spaced at 0.5 orders of magnitude Laitinen et al. 2023) as a function of $\Delta\phi$. The arrival times, and hence the path lengths, of the protons are determined as the time when the intensity reaches 1% of the global maximum intensity at 1 au. The dashed black curve shows the mean field line length, and the horizontal red line shows the nominal Parker spiral length. The magenta and cyan ranges at the bottom correspond to those in Fig. 1.

We investigate the first arrival and the apparent path length of the simulated SEPs at 1 au in Fig. 3. We define the onset time as the first time the SEP intensity exceeds a threshold of 1% of the global maximum intensity of the simulated event, $I = 1.5$ particles/(s °). We further converted the onset time to an apparent path length (solid blue curve in Fig. 3), for comparison with the field line lengths obtained in Laitinen et al. (2023) for the same turbulence parameters as in this study (contour lines,

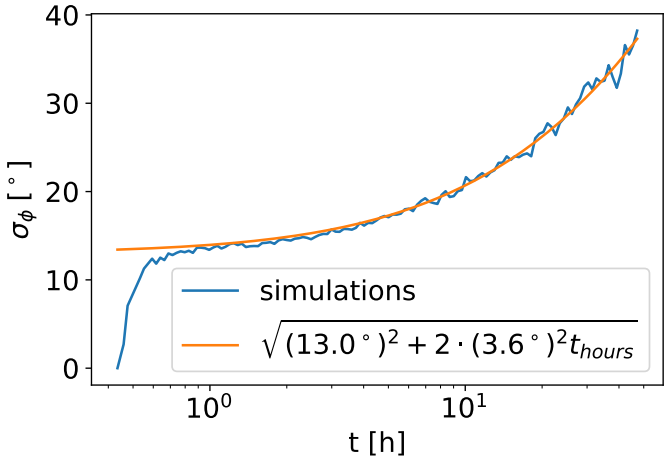

Fig. 4. Heliolongitudinal standard deviation of the 100-MeV protons as a function of time. The amber curve shows the functional form where the standard deviation is initially 13°, and then increases consistent with longitudinal diffusion with diffusion coefficient $\kappa_\phi = (3.6°)^2$/h.

with the dashed black line showing the mean field line length), and the nominal Parker spiral length (the horizontal solid red line).

As can be seen in Fig. 3, the apparent path length of the 100 MeV protons traces the general trend of the field line lengths in that within the range of $\Delta\phi = -15°$ to 15° the westward path lengths are considerably shorter than the eastward ones. However, the path lengths are 20% longer than the mean field line length (dashed black curve in Fig. 3), and 30−50% longer than the nominal Parker spiral length. At more western observer locations, $\Delta\phi < -15°$, the apparent SEP path length begins to increase, deviating from the trend of decreasing field line lengths. Similar lengthening of the apparent SEP path length, compared to the mean field line length, can be seen at eastern longitudes $\Delta\phi > 15°$.

After the rapid SEP onset at heliolongitudes $|\Delta\phi| < 40°$, the longitudinal distribution of the SEPs broadens gradually, resulting in considerably longer onset delays at wider longitudes ($|\Delta\phi| \gtrsim 40°$, see Fig. 2). The broadening of the distribution is traced in Fig. 4, showing the temporal evolution of the longitudinal standard deviation σ_ϕ of particles at 1 au (blue curve). After the rapid increase of the standard deviation to $\sigma_\phi \approx 13°$, the distribution begins to gradually widen. We fitted the standard deviation with

$$\sigma_\phi^2(t) = \sigma_{\rm FL}^2 + 2\kappa_\phi t, \quad (2)$$

which describes diffusive evolution of the variance with diffusion coefficient κ_ϕ from an initial Gaussian distribution with a standard deviation of $\sigma_{\rm FL}$. A fit done by eye gives $\sigma_{\rm FL} = 13°$, which corresponds to the standard deviation of the meandering magnetic field line distribution obtained for our turbulence parameters in Laitinen et al. (2023), and particle longitudinal diffusion coefficient $\kappa_\phi = (3.6°)^2$/h (orange curve). The close match between the two curves shows that the longitudinal evolution of the particle distribution can be described as diffusion of particles from an initial distribution that is determined by the random-walk of field lines as they traverse the distance between the Sun and 1 au. It should be noted that the above analysis does not take into account the effect of longitudinal drifts which are minimised by injecting particles at latitude 0 degrees. However, as particles move away from this latitude, some drift in longitude subsequently takes place (Dalla et al. 2013).

4. Discussion and conclusions

In this Letter, we have presented the first 3D test particle simulations of SEPs in a heliospheric configuration where the large-scale Parker spiral magnetic field is superposed with a predominantly 2D turbulent component that is 2D with respect to the background magnetic field. The turbulence model is presented in detail in Laitinen et al. (2023), where we show that the turbulently meandering field lines were significantly longer than the Parker spiral, and longer at observer locations connected eastwards from the source, as compared to westward observers (coloured contours in Fig. 3).

Laitinen et al. (2023) analysed only field line lengths, thus not accounting for the effects of the turbulence on SEP propagation along and across the meandering field lines. In this work, we have analysed the propagation of 100 MeV protons using full-orbit test particle simulations, where the transport effects due to turbulence are naturally taken into account.

We found that the protons have rapid access to a longitudinal range of 60° within tens of minutes after the first arrival of the particles to 1 au (Fig. 2). A wide range of longitudes accessed by SEPs rapidly has been reported by for example Richardson et al. (2014) and Dresing et al. (2014). The first SEPs are seen to arrive westwards from the well-connected longitude.

The effect of turbulence-induced parallel scattering is demonstrated by the difference between the apparent SEP path lengths and the length of the meandering field lines, shown in Fig. 3. The SEP path lengths derived from the simulations are 20% longer than the mean length of the field lines (Laitinen et al. 2023) within $|\Delta\phi| < 15°$, and 30−50% longer than the Parker spiral. The 20% difference we obtained results in a value of the effective pitch angle $\Theta_{\rm eff} = \arccos(s_{\rm FL}/s_{\rm SEP})$, as defined by Chhiber et al. (2021a), of 34°, where $s_{\rm FL}$ and $s_{\rm SEP}$ are the mean length of the field lines and the apparent SEP path length, respectively. Chhiber et al. (2021a) obtained $\Theta_{\rm eff} = 37°$ from analysis of Parker Solar Probe observations, and $\Theta_{\rm eff} = 25°$ using a turbulence model in radial background magnetic field geometry. Our result of $\Theta_{\rm eff} = 34°$ is consistent with these values. For larger $|\Delta\phi|$ the difference between the SEP path and field line length increases further, exceeding 30% at $|\Delta\phi| \gtrsim 30°$. The shortest SEP path length is at $\Delta\phi = -15°$; the path lengths, and thus the onset times, increase monotonically on either side of this heliolongitude (see also Fig. 2), which is consistent with the trend seen in observations (e.g. Richardson et al. 2014)[1].

The westward asymmetry in intensities continues after the onset phase, and the global maximum intensity in our simulations is reached an hour after the injection of the SEPs, at heliolongitude $\Delta\phi = -15°$. This again is consistent with observations, as fits to measured SEP peak intensities versus $\Delta\phi$ indicate a similar westward location of the maximum of the Gaussian at $\Delta\phi \sim -15°$ (Lario et al. 2013; Richardson et al. 2014).

The evolution of the width of the heliolongitudinal standard deviation has been reported in recent studies. Dresing et al. (2018) find that during the 26 December 2013 event the standard deviation of the longitudinal intensity distribution of 30−60 MeV protons increased from 35° to 50−60° in 23 h. For the evolution of the longitudinal standard deviation that follows the form given by Eq. (2) with $\sigma_{\rm FL} = 35°$, this corresponds to $\kappa_\phi \sim (6°)^2$/h. Similar values can be obtained from the analysis of four SEP events by Kahler et al. (2023) whose linear change rate of ∼10°/day is equivalent to diffusive rates $\sim(5°)^2$/h. These values are slightly higher than our results; however, they are of the

[1] It should be noted that the Richardson et al. (2014) study did not resolve the 15° displacement from $\Delta\phi = 0°$ of the shortest onset time.

same order, indicating that turbulence-induced diffusion of SEPs across the mean field, as seen in our simulations, is a possible explanation for the observed evolution of the cross-field extent of SEPs during solar events.

We conclude that several features of observed SEP events can arise naturally from the turbulent nature of the interplanetary magnetic field. This does not preclude that a wide CME source may also be contributing to wide SEP events (e.g. Reames 1999), as well as to shifting the SEP peak intensity (Lario et al. 2013; Kahler et al. 2023), and to temporally increasing the heliolongitudinal extent of an SEP event (e.g. Kouloumvakos et al. 2016).

It should be noted that the turbulence parameters determine the degree of field line meandering, and thus the initial extent of the SEP event (~60° in Fig. 2; e.g. Laitinen et al. 2017). Parameters such as those used in Laitinen et al. (2016) and Chhiber et al. (2021b) likely result in a wider extent. Further work, with a wide range of turbulence and particle source parameters, are needed to analyse the relative importance of different mechanisms in forming the observed SEP intensity evolution at different heliolongitudes.

Acknowledgements. T.L. and S.D. acknowledge support from the UK Science and Technology Facilities Council (STFC) through grants ST/R000425/1 and ST/V000934/1. C.W. and S.D. acknowledge support from NERC via the SWARM project, part of the SWIMMR programme (grant NE/V002864/1). This work was performed using resources provided by the Cambridge Service for Data Driven Discovery (CSD3) operated by the University of Cambridge Research Computing Service (www.csd3.cam.ac.uk), provided by Dell EMC and Intel using Tier-2 funding from the Engineering and Physical Sciences Research Council (capital grant EP/P020259/1), and DiRAC funding from the Science and Technology Facilities Council (www.dirac.ac.uk). T.L. acknowledges support from the International Space Science Institute through funding of the International Team #35 "Using Energetic Electron And Ion Observations To Investigate Solar Wind Structures And Infer Solar Wind Magnetic Field Configurations".

References

Agueda, N., Lario, D., Vainio, R., et al. 2009, A&A, 507, 981
Bandyopadhyay, R., & McComas, D. J. 2021, ApJ, 923, 193
Chen, C. H. K., Bale, S. D., Bonnell, J. W., et al. 2020, ApJS, 246, 53
Chhiber, R., Matthaeus, W. H., Cohen, C. M. S., et al. 2021a, A&A, 650, A26
Chhiber, R., Ruffolo, D., Matthaeus, W. H., et al. 2021b, ApJ, 908, 174
Cohen, C. M. S., Mason, G. M., Mewaldt, R. A., & Wiedenbeck, M. E. 2014, ApJ, 793, 35
Cohen, C. M. S., Mason, G. M., & Mewaldt, R. A. 2017, ApJ, 843, 132
Cuesta, M. E., Chhiber, R., Roy, S., et al. 2022, ApJ, 932, L11
Dalla, S., & Browning, P. K. 2005, A&A, 436, 1103
Dalla, S., Marsh, M. S., Kelly, J., & Laitinen, T. 2013, J. Geophys. Res.: Space Phys., 118, 5979
Desai, M. I., Mason, G. M., Dwyer, J. R., et al. 2003, ApJ, 588, 1149
Dresing, N., Gómez-Herrero, R., Heber, B., et al. 2014, A&A, 567, A27
Dresing, N., Gómez-Herrero, R., Heber, B., et al. 2018, A&A, 613, A21
Dröge, W. 2000, ApJ, 537, 1073
Dröge, W., Kartavykh, Y. Y., Klecker, B., & Kovaltsov, G. A. 2010, ApJ, 709, 912
He, H.-Q., Qin, G., & Zhang, M. 2011, ApJ, 734, 74
Hutchinson, A., Dalla, S., Laitinen, T., & Waterfall, C. O. G. 2023, A&A, 670, L24
Jokipii, J. R. 1966, ApJ, 146, 480
Kahler, S. W., Ling, A. G., & Reames, D. V. 2023, ApJ, 942, 68
Kallenrode, M. B. 1993, J. Geophys. Res., 98, 19037
Kouloumvakos, A., Patsourakos, S., Nindos, A., et al. 2016, ApJ, 821, 31
Laitinen, T., & Dalla, S. 2019, ApJ, 887, 222
Laitinen, T., Dalla, S., & Marsh, M. S. 2013, ApJ, 773, L29
Laitinen, T., Kopp, A., Effenberger, F., Dalla, S., & Marsh, M. S. 2016, A&A, 591, A18
Laitinen, T., Dalla, S., & Marriott, D. 2017, MNRAS, 470, 3149
Laitinen, T., Effenberger, F., Kopp, A., & Dalla, S. 2018, J. Space Weather Space Clim., 8, A13
Laitinen, T., Dalla, S., Waterfall, C. O. G., & Hutchinson, A. 2023, ApJ, 943, 108
Lario, D., Kallenrode, M.-B., Decker, R. B., et al. 2006, ApJ, 653, 1531
Lario, D., Aran, A., Gómez-Herrero, R., et al. 2013, ApJ, 767, 41
Leske, R. A., Christian, E. R., Cohen, C. M. S., et al. 2020, ApJS, 246, 35
Liewer, P. C., Neugebauer, M., & Zurbuchen, T. 2004, Sol. Phys., 223, 209
Marsh, M. S., Dalla, S., Kelly, J., & Laitinen, T. 2013, ApJ, 774, 4
Mason, G. M., Mazur, J. E., & Dwyer, J. R. 1999, ApJ, 525, L133
Moradi, A., & Li, G. 2019, ApJ, 887, 102
Paassilta, M., Raukunen, O., Vainio, R., et al. 2017, J. Space Weather Space Clim., 7, A14
Paassilta, M., Papaioannou, A., Dresing, N., et al. 2018, Sol. Phys., 293, 70
Palmer, I. D. 1982, Rev. Geophys. Space Phys., 20, 335
Parker, E. N. 1958, ApJ, 128, 664
Pei, C., Jokipii, J. R., & Giacalone, J. 2006, ApJ, 641, 1222
Reames, D. V. 1999, Space Sci. Rev., 90, 413
Richardson, I. G., von Rosenvinge, T. T., Cane, H. V., et al. 2014, Sol. Phys., 289, 3059
Schrijver, C. J., & Title, A. M. 2011, J. Geophys. Res.: Space Phys., 116, A04108
Strauss, R. D., & Fichtner, H. 2015, ApJ, 801, 29
Torsti, J., Kocharov, L. G., Vainio, R., Anttila, A., & Kovaltsov, G. A. 1996, Sol. Phys., 166, 135
Wiedenbeck, M. E., Mason, G. M., Cohen, C. M. S., et al. 2013, ApJ, 762, 54
Zhang, M., Qin, G., & Rassoul, H. 2009, ApJ, 692, 109